Bloch mode engineering in graphene modulated periodic waveguides and cavities

Chengzhi Qin,[1] Bing Wang,[1,*] Hua Long,[1] Kai Wang,[1] and Peixiang Lu[1,2]

[1]Wuhan National Laboratory for Optoelectronics and School of Physics, Huazhong University of Science and Technology, Wuhan 430074, China
[2]Laboratory for Optical Information Technology, Wuhan Institute of Technology, Wuhan 430074, China
*Corresponding author: wangbing@hust.edu.cn

We present an approach to engineer Bloch modes by using monolayer graphene decorated on the surfaces of periodic waveguides or incorporated in cavities. In the terahertz and far-infrared ranges, the presence of graphene brings about a tunable band shift to Bloch modes in periodic waveguides. Thus, propagating Bloch modes may become evanescent and vice versa for both TE and TM polarizations. The resonant wavelength in the cavities experiences a linear dependence on the graphene chemical potential, which also has an effect on the field localization and enhancement of the cavity modes. This study suggests that graphene modulated periodic waveguides and cavities may find great applications in terahertz ranges like tunable filters, switches, and modulators. ©2015 Optical Society of America

1. INTRODUCTION

It is an important issue to manipulate light propagation and confinement for optical processing and connecting in integrated optics [1]. Periodic waveguides, unlike the traditional z-invariant waveguides, can form photonic bandgaps due to the periodic index distributions along the propagation direction [2]. By engineering the dispersion relation, one can modulate the properties of Bloch modes in periodic waveguides, such as yielding slow group velocities and anomalous dispersion [3,4]. In addition, cavities can be constructed by introducing defects in the periodic waveguides. The defect can support a localized resonant mode and trap light in a volume of subwavelength scale. Since the mode resonance in the cavities is highly sensitive to the surrounding environment, one has to utilize tunable materials such as graphene to control the resonance condition, with the aim of finding applications in ultrafast optical switches and highly sensitive optical sensors [5,6].

As a two-dimensional material [7], graphene has almost no structural effect on the original waveguides and cavities; it is ready to be integrated with traditional photonic devices. In the infrared and terahertz (THz) ranges, graphene behaves like a noble metal in the visible range and can support surface plasmon polaritons (SPPs) [8,9]. Recently, graphene has been investigated in combination with traditional devices for many terahertz applications, such as tunable hyperbolic metamaterials [10], terahertz absorbers [11,12], and subdiffraction imaging hyperlenses [13]. Moreover, the flexible and broadband tunability makes graphene a prospective material to tailor

light propagation [14,15]. In addition, the current development of large-scale growth and transfer techniques of graphene ensures its integration with the existing photonic platform [16,17].

In this work, we shall employ graphene to engineer Bloch modes in periodic waveguides and cavities. First, we consider that the graphene is decorated on the surfaces of the periodic waveguides. As Bloch modes are formed by propagating waves scattered forward and backward many times in the periodic waveguides, such a configuration could enhance the interaction between light and graphene. We also incorporate graphene in the cavities formed by introducing defects in the periodic waveguides. The enhanced localized field of the resonant mode could also facilitate the coupling of light and graphene, leading to the strong modulation of the Bloch modes.

2. BLOCH MODE ENGINEERING WITH GRAPHENE IN PERIODIC WAVEGUIDES

We start by studying the graphene modulated periodic waveguide. As shown in Fig. 1(a), the waveguide consists of air grooves periodically etched into a silicon slab on a polytetrafluoroethylene (PTFE) substrate [18]. The surfaces of the periodic waveguide, parallel and perpendicular to the propagation direction, are coated with monolayer graphene. The numerical results presented throughout the paper are obtained with the aperiodic-Fourier modal method (a-FMM) [19,20]. In the calculation, graphene is modeled as an ultrathin and dispersive film with a thickness of $\Delta = 1$ nm and an equivalent bulk

permittivity of $\epsilon_{g,eq} = 1 + i\sigma_g\eta_0/(k_0\Delta)$ [21]. The surface conductivity of graphene σ_g is governed by the Kubo formula [22] as a function of photon frequency ω, chemical potential μ_c, momentum relaxation time τ, and temperature T. $\tau = \mu\mu_c/(ev_F^2)$, with e being the electron charge and $v_F = 10^6$ m/s the Fermi velocity. Here, we choose the impurity-limited DC mobility $\mu = 10,000$ cm^2/Vs at room temperature $T = 300$ K, which is in accordance with the experimental results [23].

The band diagrams of the fundamental Bloch modes in the periodic waveguides without (red curves) and with (blue curves) graphene are illustrated in Figs. 1(b)–1(e). Figures 1(b) and 1(c) denote TE polarization (E_y, H_x, H_z, with E_y parallel to the groove), while Figs. 1(d) and 1(e) represent TM polarization (H_y, E_x, E_z, with H_y parallel to the groove). The presence of graphene brings about a blue band shift to the fundamental Bloch modes for both TE and TM polarizations. For TE polarization, as the bottom of the conduction band experiences a more obvious blueshift than the top of the valence band as graphene is introduced, the bandgap is enlarged, while for TM polarization, the blueshift at the top of valence band becomes more obvious, making the bandgap become narrower. The mechanism behind the blue band shifts
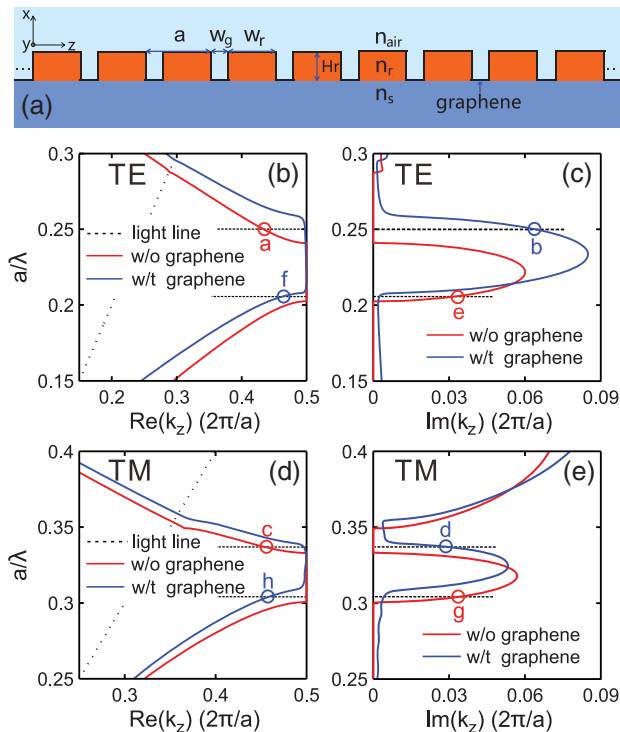

Fig. 1. Schematics of graphene modulated periodic waveguides and band diagrams of fundamental Bloch modes with and without graphene. (a) The refractive indices are $n_r = 3.42$, $n_{air} = 1.0$, and $n_s = 1.4$. The period is $a = 10$ μm with $W_r = 8$ μm, $W_g = 2$ μm, and $H_r = 5$ μm. Real and imaginary parts of the Bloch wave vectors (b) and (c) for TE polarization and (d) and (e) for TM polarization. The gray dashed lines in (b) and (d) denote the light lines beneath which guided Bloch modes exist. The red and blue circles denoted by a–h represent the particular frequencies near the edges of the bandgaps. The graphene chemical potential is $\mu_c = 0.5$ eV.

can be qualitatively explained from the effective medium approximation (EMA) point of view [10,24]. As the operation wavelength (of orders of 50 μm) is much larger than the waveguide period (10 μm), the periodic waveguide can be equivalent to a homogeneous medium. In the absence of graphene, the effective permittivity $\epsilon_{eff,w/o}$ of the periodic waveguide satisfies $1 = \epsilon_{air} < \epsilon_{eff,w/o} < \epsilon_r = 3.42^2$. As graphene is introduced, the effective permittivity becomes $\epsilon_{eff,w/t} = \epsilon_{eff,w/o} + i\sigma_g\eta_0/(k_0 w_{eff})$, with w_{eff} being the effective mode width. In THz and far-infrared ranges ($\hbar\omega < |2\mu_c|$), the intraband transition process dominates and graphene manifests a Drude-like surface conductivity [25,26] $\sigma_g = ie^2\mu_c/[\pi\hbar^2(\omega + i\tau^{-1})]$. As Im($\sigma_g$) > 0, we have Re($\epsilon_{eff,w/t}$) < Re($\epsilon_{eff,w/o}$). Since the real part of the Bloch wave vector is positively correlated with the effective permittivity, the Bloch wave vectors satisfy $k_0 < $ Re($k_{z,w/t}$) < Re($k_{z,w/o}$) < $\sqrt{\epsilon_r}k_0$ in the valence and conduction bands. So the presence of graphene could bring about blue band shifts to the fundamental Bloch modes.

In the bandgaps, the imaginary parts of the Bloch wave vectors increase for TE polarization and decrease for TM polarization where graphene exists. In the valence or conduction bands below the light lines without graphene, the imaginary parts of the Bloch wave vectors vanish. Thus, the modes experience no propagation loss. While in the presence of graphene, very tiny but nonzero values of the imaginary parts of the Bloch wave vectors emerge. Due to the intrinsic loss of graphene caused by the intraband transition in the terahertz ranges, the Bloch modes also experience a tiny propagation loss as they interact with graphene. As the band curves intersect the light lines, the fundamental Bloch modes become leaky and cause considerable propagation loss. Note that the presence of graphene pushes up the dispersion curves. The lower frequency limits for the emerging leaky Bloch modes lift accordingly.

Figure 2 illustrates the normalized field intensity distributions of the fundamental Bloch modes at the frequencies denoted by a–h in Fig. 1. In the vicinity of the bottoms of the conduction bands for both TE and TM polarizations shown in Figs. 2(a)–2(d), the periodic waveguides support propagating and evanescent Bloch modes with and without graphene, respectively. As the presence of graphene pushes up the bottoms of the conduction bands, the frequency regimes from $a/\lambda = 0.24$ to 0.26 for TE and $a/\lambda = 0.333$ to 0.343 for TM polarizations transform from the conduction to the forbidden bands, making the modes in the ranges change from propagating to evanescent. In contrast, near the top of the valence bands shown in Figs. 2(e)–2(h), the Bloch modes in the ranges from $a/\lambda = 0.202$ to 0.207 for TE and $a/\lambda = 0.30$ to 0.307 for TM polarizations can be tuned from evanescent to propagating. The interaction strengths between the graphene and the Bloch modes differ from the graphene on the upper surfaces to those on the side surfaces of the periodic waveguides. At the bottoms of the conduction bands for TE polarization shown in Figs. 2(a) and 2(b), the Bloch mode energy is concentrated in the grooves of the periodic waveguides. As $|E_{y,side}| > |E_{y,upper}|$, the graphene on the side surfaces plays a leading role when interacting with the Bloch modes. At the
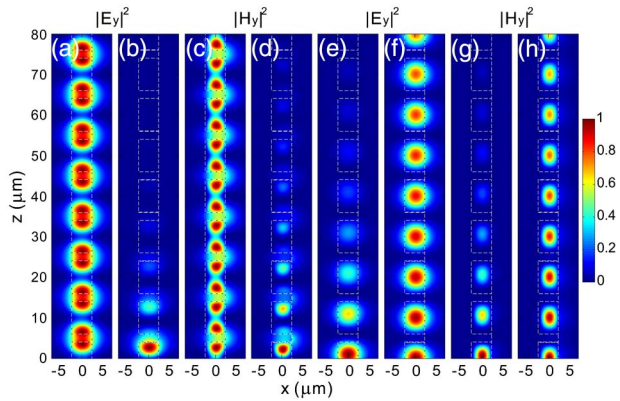
Fig. 2. Normalized field intensity distributions of the fundamental Bloch modes at frequencies denoted by a–h in Fig. 1. (a) and (b) $|E_y|^2$ distributions at $a/\lambda = 0.25$ for TE polarization. (c) and (d) $|H_y|^2$ distributions at $a/\lambda = 0.337$ for TM polarization. (e) and (f) $|E_y|^2$ distributions at $a/\lambda = 0.206$ for TE polarization. (g) and (h) $|H_y|^2$ distributions at $a/\lambda = 0.304$ for TM polarization. In (a), (c), (e), and (g), graphene does not exist. In (b), (d), (f), and (h), graphene is coated on the surfaces of the periodic waveguides.

Fig. 3. Band diagrams of the fundamental Bloch modes without graphene and at the presence of graphene as $\mu_c = 0.1$, 0.3, 0.5, and 0.7 eV. Real and imaginary parts of Bloch wave vectors (a) and (b) for TE polarization and (c) and (d) for TM polarization.

top of the valence bands with the mode energy concentrated in the ridges of the periodic waveguides shown in Figs. 2(e) and 2(f), since $|E_{y,\mathrm{upper}}| > |E_{y,\mathrm{side}}|$, the graphene on the upper surfaces has greater influence on the Bloch modes than that on the side surfaces. For TM polarization, as E_x and E_z components of the Bloch modes induce surface currents on the graphene at the side and upper surfaces, respectively. So the graphene on the respective surfaces has different influences on the Bloch modes.

In Fig. 3, we plot the band diagrams of the fundamental Bloch modes without graphene and with graphene as $\mu_c = 0.1$, 0.3, 0.5, and 0.7 eV. It shows that a larger chemical potential of graphene could bring about a more obvious blueshift to the band diagrams. For TE polarization shown in Figs. 3(a) and 3(b), the bottoms of the conduction bands manifest a continuous blueshift from $a/\lambda = 0.241$ (41.5 μm) to 0.263 (38.0 μm). Meanwhile, the imaginary parts of the Bloch wave vectors are nearly doubled as $\mu_c = 0.7$ eV with respect to that without graphene. In contrast to TE polarization, both the bandgaps and the imaginary parts of Bloch wave vectors for TM polarization shrink as μ_c increases. The influence of μ_c on the Bloch modes is determined by the optical response of graphene within the present frequencies. In THz and far-infrared ranges, graphene manifests a Drude-like surface conductivity $\sigma_g = ie^2 \mu_c / [\pi \hbar^2 (\omega + i\tau^{-1})]$. Since σ_g is proportional to μ_c, the interaction between Bloch modes and graphene could be enhanced by increasing the chemical potential. As graphene modulated periodic waveguides are applied to tunable band stop filters, both the center wavelength and bandwidth could be tuned continuously by varying the chemical potential of the coated graphene.

It is interesting to investigate the influence of graphene on the metal periodic waveguides. Recent studies [27,28] have shown that spoof SPPs can propagate along the periodically corrugat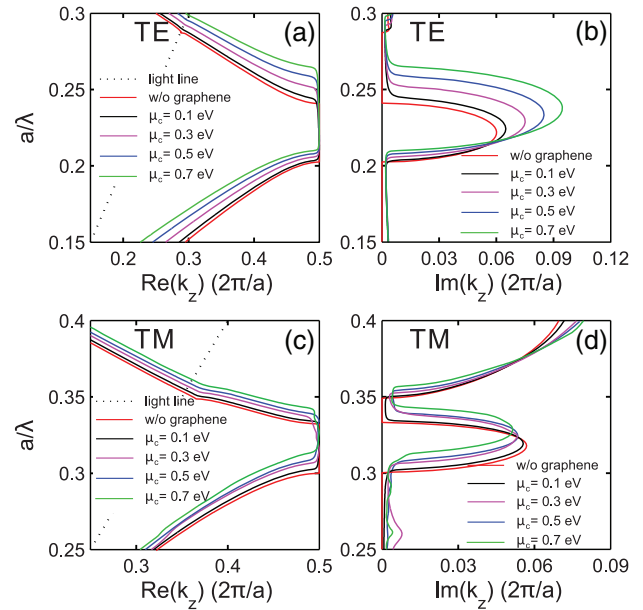ed surfaces in THz and far-infrared ranges. The dispersion relation of these surface Bloch modes is mainly engineered by the geometry of the corrugation. Since graphene is a 2D material with only one atomic thickness, the influence of graphene on spoof SPPs is negligible. In visible ranges, the presence of graphene on the metal surfaces can increase the propagation loss of metal SPPs. In this work, we will focus our discussion on the influence of graphene on dielectric periodic waveguides.

3. GRAPHENE MODULATED CAVITIES

Now we consider the graphene modulated cavities. As shown in Fig. 4(a), the cavity is constructed by changing the ridge length of the center unit cell of the periodic waveguides. The inside walls of the cavity are covered by monolayer graphene. The whole structure is illuminated by the fundamental mode of the slab waveguide from the left side. With the periodic cells at both sides acting as Bragg mirrors, the cavity can support a localized resonant mode. The transmission spectra of the cavity are calculated numerically with the a-FMM and a semi-analytical method [29]. Here, we denote Φ_1 and Φ_{-1} as the fundamental modes propagating forward and backward in the slab waveguides, respectively. $\mathbf{B}_1$, $\mathbf{B}_{-1}$ and $\mathbf{B}'_1$, $\mathbf{B}'_{-1}$ are the counter-propagating fundamental Bloch modes in the periodic waveguides and the cavities, respectively. Considering the boundary conditions at each interface, we have

$$\begin{cases} \Phi_1 + r_{-1}\Phi_{-1} = a_1 \mathbf{B}_1 + a_{-1}\mathbf{B}_{-1} \\ a_1 u_1 \mathbf{B}_1 + a_{-1} u_{-1} \mathbf{B}_{-1} = b_1 \mathbf{B}'_1 + b_{-1}\mathbf{B}'_{-1} \\ b_1 u'_1 \mathbf{B}'_1 + b_{-1} u'_{-1} \mathbf{B}'_{-1} = c_1 \mathbf{B}_1 + c_{-1}\mathbf{B}_{-1} \\ c_1 u_1 \mathbf{B}_1 + c_{-1} u_{-1} \mathbf{B}_{-1} = t_1 \Phi_1 \end{cases}, \quad (1)$$

where r_{-1}, t_1, a_1, a_{-1}, b_1, b_{-1}, c_1, c_{-1} represent the corresponding mode amplitudes. $u_1 = \exp(ik_{z,1}L_p)$, $u_{-1} = \exp(-ik_{z,1}L_p)$,
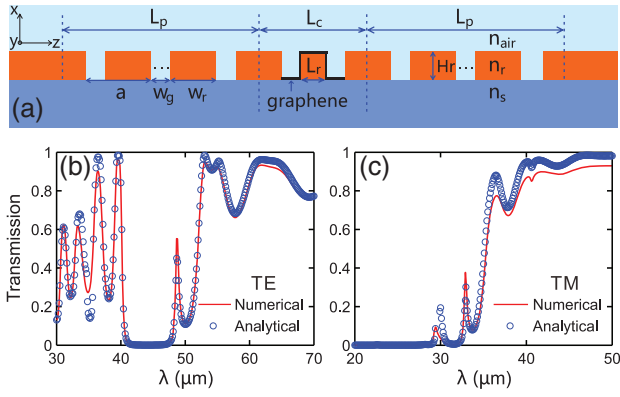
Fig. 4. Schematic and transmission spectra of the graphene modulated cavity. (a) L_c, L_p are the lengths of the cavity and the periodic waveguide (with five periods at each side), with L_r being the center ridge length. Graphene is decorated on the cavity inside walls. The periodic waveguides are connected with monomode slab waveguides at both sides. (b) and (c) Transmission spectra of the cavity for TE and TM polarizations. Red curves and blue circles represent the numerical and analytical results. (b) $L_r = 0.8 W_r$. (c) $L_r = 1.8 W_r$. μ_c is fixed at 0.5 eV.

$u_1' = \exp(ik_{z,1}' L_c)$, and $u_1' = \exp(-ik_{z,1}' L_c)$ with $k_{z,1}$, $k_{z,1}'$ being the fundamental Bloch wave vectors and L_p, L_c the lengths of the periodic waveguide and the cavity, respectively. To solve Eq. (1), we perform generalized inner products with $\boldsymbol{\Phi}_1$ and $\boldsymbol{\Phi}_{-1}$ by applying the Bloch mode orthogonality condition [30,31], and we yield

$$\langle \boldsymbol{\Phi}_m, \boldsymbol{\Phi}_{-n} \rangle = \iint_S (\mathbf{E}_m \times \mathbf{H}_{-n} - \mathbf{E}_{-n} \times \mathbf{H}_m) \cdot \hat{z} \, dS = F \delta_{m,n} \quad (2)$$

with $\boldsymbol{\Phi}_m = |\mathbf{E}_m, \mathbf{H}_m\rangle \exp(ik_m z)$, $\boldsymbol{\Phi}_{-n} = |\mathbf{E}_{-n}, \mathbf{H}_{-n}\rangle \exp(ik_{-n} z)$, and $\delta_{m,n}$ is 1 for m = n and 0 otherwise. F is a complex constant used for normalizing the modes (here, we choose $F = 1$). We obtain the modal lectance and transmittance $R_1 = |r_{-1}|^2$ and $T_1 = |t_1|^2$.

The transmission spectra of the graphene modulated cavity for both TE and TM polarizations are illustrated in Figs. 4(b) and 4(c). The red curves represent the numerical results and the blue circles denote the analytical data; they agree well with each other. As we only consider the fundamental Bloch modes in the analytical calculation while all Bloch modes (guided and leaky) are included in the numerical simulations, the spectrum coincidence indicates that most of the electromagnetic energy is transported by the fundamental Bloch modes. Particularly, for TE polarization, the resonant peak of the cavity locates at $\lambda_m = 48.7$ μm, with the transmittance reaching 60%. For TM polarization, the resonant peak locates at $\lambda_m = 32.9$ μm, which is near the top of the valence band of the periodic waveguides.

The transmission spectra of the cavity can be tuned by cavity geometry or graphene chemical potential. In Figs. 5(a) and 5(b), the resonant peaks both exhibit redshifts as the cavity ridge lengths L_r increase. For the TE polarization shown in Fig. 5(a), the resonant peaks have shifts of $\lambda_m = 41$–49 μm, which covers the whole bandgap of the periodic waveguides and manifests a strong modulation of the transmission
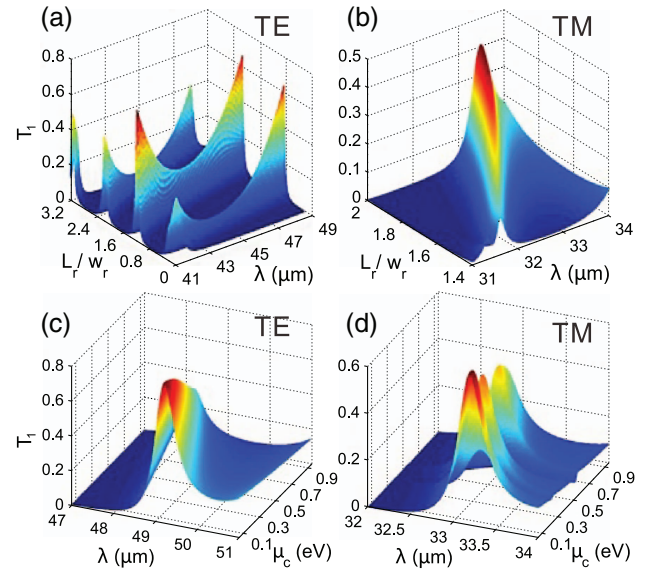

Fig. 5. Influences of cavity ridge length L_r and graphene chemical potential μ_c on the transmission spectra. (a) and (c) TE polarization. (b) and (d) TM polarization. (a) and (b) Transmission spectra tuned by ridge length L_r at fixed $\mu_c = 0.5$ eV. (a) $L_r \in [0.2 W_r, 3.2 W_r]$ and (b) $L_r \in [1.4 W_r, 2.0 W_r]$. (c) and (d) Transmission spectra tuned by graphene chemical potential $\mu_c \in [0.05 \text{ eV}, 0.95 \text{ eV}]$ for different ridge lengths. (c) $L_r = 0.8 W_r$ and (d) $L_r = 1.8 W_r$.

spectrum. The three series of resonant peaks correspond to the first- to third-order longitudinal modes, the transmittances of which all decrease to the minima near the center of the bandgaps and increase to the maxima at the tops of the valence bands. For the TM polarization shown in Fig. 5(b), the resonant peak experiences a redshift of $\lambda_m = 31.6$–33.5 μm with the transmittance at λ_m increasing significantly from 13.4% to 40% as the cavity length increases. Figures 5(c) and 5(d) show the transmission spectra as μ_c increases from 0.05 to 0.95 eV. In general, the resonant peaks manifest linear dependences on the chemical potential. For TE polarization, the resonant peak shifts linearly from $\lambda_m = 49.2$ to 48.2 μm with the transmittance at λ_m decreasing from $T_1 = 80\%$ to 30%. For the TM polarization shown in Fig. 5(d), the resonant peaks also experience blueshifts as μ_c increases, but the tuning ranges are narrower than those of TE polarization.

The red (or blue) shift of the cavity resonant wavelength can also be understood in terms of the EMA point of view. The resonant wavelength satisfies the Fabry–Perot condition [32] $\arg(r_b) + 2\pi n_{eff} L_{eff,c}/\lambda_m = 2m\pi$, with $n_{eff} = \text{Re}(\sqrt{\epsilon_{eff}})$. Here, ϵ_{eff} and $L_{eff,c}$ are the effective permittivity and length of the cavity, respectively, and r_b is the Bragg reflection coefficient of the periodic waveguides beside the cavity. λ_m is the resonant wavelength with m being the order of the longitudinal mode. As we increase the cavity ridge length L_r at fixed μ_c, both $\epsilon_{eff,w/t}$ and $L_{eff,c}$ are increased. To satisfy the resonant condition, the resonant wavelength λ_m will experience a redshift. For $\mu_c \in [0.05 \text{ eV}, 0.95 \text{ eV}]$ at fixed cavity ridge length L_r, since $\text{Im}(\sigma_g) \propto \mu_c$, the real part of the cavity effective permittivity $\text{Re}(\epsilon_{eff,w/t}) = \text{Re}(\epsilon_{eff,w/o}) - \text{Im}(\sigma_g)\eta_0/(k_0 w_{eff})$ will decrease as μ_c increases. Noting that both $L_{eff,c}$ and $\arg(r_b)$ are fixed,

the resonant wavelength λ_m will experience a blueshift. We also calculate the cavity transmission spectra without graphene and with graphene at $\mu_c = 0$ eV, both of which manifest very slight differences with that of $\mu_c = 0.05$ eV. As for $\mu_c = 0$ eV($\hbar\omega > |2\mu_c|$), the interband transition process dominates and graphene possesses a constant surface conductivity $\sigma_g \approx e^2/(4\hbar)$ [7,26] with a near-zero imaginary part $\text{Im}(\sigma_g)$, making the effective permittivity $\text{Re}(\epsilon_{\text{eff,w/t}})$ nearly unchanged. So the presence of graphene has negligible influence on the cavity resonant wavelength. In this paper, we only consider the intraband regime ($\hbar\omega < |2\mu_c|$) within which a Drude-like model of graphene is applicable.

The Q-factor can be obtained from the transmission spectrum of the cavity which is given by $Q = \lambda_m/\Delta\lambda$ [33], with λ_m being the resonant wavelength and $\Delta\lambda$ the full width at half-maximum. In the absence of graphene, the Q-factor is $Q = 84.9$. As graphene is introduced, the Q-factors become $Q = 76.5$, 88.5, and 89.1 at $\mu_c = 0.05$, 0.5, and 0.95 eV. The Q-factor is limited by the intrinsic loss of graphene and the radiative loss of the cavity. As the intrinsic loss is determined by the electron relaxation time of graphene $\tau = \mu\mu_c/(ev_F^2)$, we can increase τ to reduce the loss. In practice, one can improve the carrier mobility μ by controlling the graphene charge environment such as by placing organic molecules and nanoparticles near the graphene [34]. We can also increase τ by increasing the chemical potential μ_c via electric gating and chemical doping. In addition, gain material may also be employed in the cavity to compensate for the loss of graphene. The cavity radiative losses consist of two decay mechanisms [2]: the energy can decay into the periodic waveguides beside the cavity or radiate into the cladding and substrate. The Q-factors can be improved by increasing the number of periods beside the cavity to increase the Bragg reflection of periodic waveguides. The out-of-plane radiating loss can be reduced by choosing the substrate with a low refractive index.

In Fig. 6, we simulate the first- to third-order longitudinal resonant modes for TE polarization. Figure 6(a) denotes the axial field distributions of the first-order longitudinal mode for $L_r = 0.8W_r$ as $\mu_c = 0.05$ and 0.95 eV, respectively. The field intensity decays exponentially from the cavity centers to both sides, and the decay rate is larger for $\mu_c = 0.95$ eV than that of $\mu_c = 0.05$ eV, making the former possess a smaller cavity mode volume. The field intensity enhancements, the ratio of the intensity maxima in the cavity center to the mode intensities in the output slab waveguides, are 20 and 46 times as $\mu_c = 0.05$ and 0.95 eV. In Fig. 6(b), the ridge length increase to $L_r = 1.8W_r$ to support the second longitudinal mode. The field intensity enhancements are 48 and 107 times as $\mu_c = 0.05$ and 0.95 eV. For the third-order longitudinal mode as $L_r = 2.6W_r$, the field intensity enhancements become 88 and 94 times as $\mu_c = 0.05$ and 0.95 eV. It shows that a larger chemical potential of graphene will facilitate the field localization of the cavity modes, and the intensity enhancement effects are obvious for lower order longitudinal modes than higher order ones. As the resonant mode can confine the electromagnetic energy in the subwavelength scale to enhance the light–matter interaction and the resonant condition is sensitive to the surrounding environment, the graphene modulated cavity may
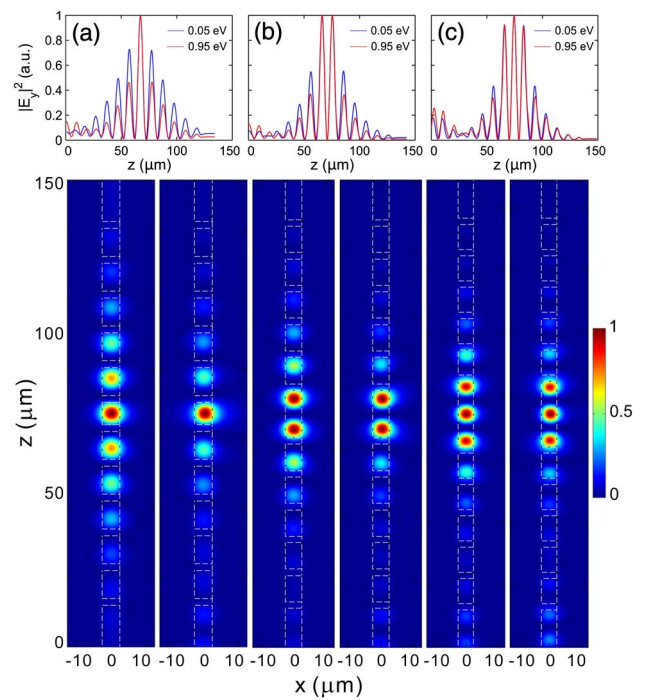

Fig. 6. Normalized $|E_y|^2$ distributions of the first- to third-order longitudinal cavity modes for TE polarization. The top blue curves and the bottom figures represent the axial mode profiles at $x = 0$ and the corresponding two-dimensional field distributions. (a) $L_r = 0.8W_r$, $\lambda_m = 49.2$ and 48.2 µm for $\mu_c = 0.05$ and 0.95 eV. (b) $L_r = 1.8W_r$, $\lambda_m = 47.6$ and 45.9 µm for $\mu_c = 0.05$ and 0.95 eV. (c) $L_r = 2.6W_r$, $\lambda_m = 44.8$ and 43.2 µm for $\mu_c = 0.05$ and 0.95 eV.

find wide applications in optical sensing. Since graphene manifests good temperature stability, the optical sensors can operate normally over a wide temperature range.

In terms of experimental implementations of the graphene modulated periodic waveguides and cavities, the coated graphene could be grown by chemical vapor deposition (CVD) and then mechanically transferred onto the surfaces of the waveguides or cavities [35]. It is also important to consider the influence of bending of graphene on its properties. Bending at the edges of waveguides might break the graphene or produce defects on the graphene, which could invalidate the material description of planar graphene [36,37]. The local Fermi energy (chemical potential) of monolayer graphene is inversely proportional to curvature radius of bending [38], and only a curvature radius of less than about 10 nm at the edges can have a substantial effect on the surface conductivity of graphene. As both the operation wavelength (∼50 µm) and the waveguide period (10 µm) are much larger than the typical curvature radius, the influence of local bending of graphene could be negligible. In practice, the sharp edges of the waveguides can be smoothed by etching techniques to further reduce the effects of bending.

4. CONCLUSIONS

In conclusion, we have investigated the Bloch mode propagation and confinement engineered by monolayer graphene

decorated on the surfaces of periodic waveguides or incorporated in the cavity. The multiple scattering of waves in the periodic waveguides or cavities yields the strong interaction of light and graphene, leading to the strong modulation of the Bloch modes. The presence of graphene brings about a blueshift to the band structure. By varying the frequencies, the propagating modes may become evanescent and vice versa. Moreover, the cavity transmission spectra can be tuned either by the cavity length or graphene chemical potential. The increase of the cavity length can give rise to a redshift in the resonant wavelength, which also undergoes a linear dependence on the graphene chemical potential. By increasing the chemical potential, one can facilitate the field localization and enhancement of the cavity modes. The study suggests that the graphene modulated periodic waveguides and cavities may find great applications in tunable THz filters, sensors, and modulators.

REFERENCES

1. C. Koos, P. Vorreau, T. Vallaitis, P. Dumon, W. Bogaerts, R. Baets, B. Esembeson, I. Biaggio, T. Michinobu, F. Diederich, W. Freude, and J. Leuthold, "All-optical high-speed signal processing with silicon-organic hybrid slot waveguides," Nat. Photonics **3**, 216–219 (2009).
2. J. D. Joannopoulos, S. G. Johnson, J. N. Winn, and R. D. Meade, *Photonic Crystals Molding the Flow of Light* (Princeton University, 2008).
3. T. Baba, "Slow light in photonic crystals," Nat. Photonics **2**, 465–473 (2008).
4. V. A. Pogrebnyak, E. Akray, and A. N. Küçükaltun, "Tunable gap in the transmission spectrum of a periodic waveguide," Appl. Phys. Lett. **86**, 151115 (2005).
5. M. Furchi, A. Urich, A. Pospischil, G. Lilley, K. Unterrainer, H. Detz, P. Klang, A. M. Andrews, W. Schrenk, G. Strasser, and T. Mueller, "Microcavity-integrated graphene photodetector," Nano Lett. **12**, 2773–2777 (2012).
6. X. Gan, K. F. Mak, Y. Gao, Y. You, F. Hatami, J. Hone, T. F. Heinz, and D. Englund, "Strong enhancement of light–matter interaction in graphene coupled to a photonic crystal nanocavity," Nano Lett. **12**, 5626–5631 (2012).
7. A. N. Grigorenko, M. Polini, and K. S. Novoselov, "Graphene plasmonics," Nat. Photonics **6**, 749–758 (2012).
8. S. Mikhailov and K. Ziegler, "New electromagnetic mode in graphene," Phys. Rev. Lett. **99**, 016803 (2007).
9. B. Wang, X. Zhang, F. J. García-Vidal, X. Yuan, and J. Teng, "Strong coupling of surface plasmon polaritons in monolayer graphene sheet arrays," Phys. Rev. Lett. **109**, 073901 (2012).
10. M. A. K. Othman, C. Guclu, and F. Capolino, "Graphene-based tunable hyperbolic metamaterials and enhanced near-field absorption," Opt. Express **21**, 7614–7632 (2013).
11. M. Amin, M. Farhat, and H. Bagci, "An ultra-broadband multilayered graphene absorber," Opt. Express **21**, 29938–29948 (2013).
12. S. Ke, B. Wang, H. Huang, H. Long, K. Wang, and P. Lu, "Plasmonic absorption enhancement in periodic cross-shaped graphene arrays," Opt. Express **23**, 8888–8900 (2015).
13. T. Zhang, L. Chen, and X. Li, "Graphene-based tunable broadband hyperlens for far-field subdiffraction imaging at mid-infrared frequencies," Opt. Express **21**, 20888–20899 (2013).
14. C. Qin, B. Wang, H. Huang, H. Long, K. Wang, and P. Lu, "Low-loss plasmonic supermodes in graphene multilayers," Opt. Express **22**, 25324–25332 (2014).
15. B. Wang, H. Huang, K. Wang, H. Long, and P. Lu, "Plasmonic routing in aperiodic graphene sheet arrays," Opt. Lett. **39**, 4867–4870 (2014).
16. K. S. Kim, Y. Zhao, H. Jang, S. Y. Lee, J. M. Kim, K. S. Kim, J. H. Ahn, P. Kim, J. Y. Choi, and B. H. Hong, "Large-scale pattern growth of graphene films for stretchable transparent electrodes," Nature **457**, 706–710 (2009).
17. Z. Sun, Z. Yan, J. Yao, E. Beitler, Y. Zhu, and M. Tour, "Growth of graphene from solid carbon sources," Nature **468**, 549–552 (2010).
18. M. Walther, A. Ortner, H. Meier, U. Löffelmann, P. J. Smith, and J. G. Korvink, "Terahertz metamaterials fabricated by inkjet printing," Appl. Phys. Lett. **95**, 251107 (2009).
19. Q. Cao, P. Lalanne, and J. P. Hugonin, "Stable and efficient Bloch-mode computational method for one-dimensional grating waveguides," J. Opt. Soc. Am. A **19**, 335–338 (2002).
20. B. Wang, S. Mazoyer, J. P. Hugonin, and P. Lalanne, "Backscattering in monomode periodic waveguides," Phys. Rev. B **78**, 245108 (2008).
21. B. Wang, X. Zhang, X. Yuan, and J. Teng, "Optical coupling of surface plasmons between graphene sheets," Appl. Phys. Lett. **100**, 131111 (2012).
22. P. Y. Chen and A. Alù, "Atomically thin surface cloak using graphene monolayers," ACS Nano **5**, 5855–5863 (2011).
23. K. S. Novoselov, A. K. Geim, S. V. Morozov, D. Jiang, Y. Zhang, S. V. Dubonos, I. V. Grigorieva, and A. A. Firsov, "Electric field effect in atomically thin carbon films," Science **306**, 666–669 (2004).
24. C. Guclu, S. Campione, and F. Capolino, "Hyperbolic metamaterial as super absorber for scattered fields generated at its surface," Phys. Rev. B **86**, 205130 (2012).
25. M. Jablan, H. Buljan, and M. Soljačić, "Plasmonics in graphene at infrared frequencies," Phys. Rev. B **80**, 245435 (2009).
26. B. Wang, X. Zhang, K. Ping Loh, and J. Teng, "Tunable broadband transmission and phase modulation of light through graphene multilayers," J. Appl. Phys. **115**, 213102 (2014).
27. S. Maier, S. Andrews, L. Martín-Moreno, and F. García-Vidal, "Terahertz surface plasmon-polariton propagation and focusing on periodically corrugated metal wires," Phys. Rev. Lett. **97**, 176805 (2006).
28. A. I. Fernández-Dominguez, L. Martin-Moreno, F. J. Garcia-Vidal, S. R. Andrews, and S. A. Maier, "Spoof surface plasmon polariton modes propagating along periodically corrugated wires," IEEE J. Sel. Top. Quantum Electron. **14**, 1515–1521 (2008).
29. W. Śmigaj, P. Lalanne, J. Yang, T. Paul, C. Rockstuhl, and F. Lederer, "Closed-form expression for the scattering coefficients at an interface between two periodic media," Appl. Phys. Lett. **98**, 111107 (2011).
30. G. Lecamp, J. P. Hugonin, and P. Lalanne, "Theoretical and computational concepts for periodic optical waveguides," Opt. Express **15**, 11042–11060 (2007).
31. T. Paul, C. Menzel, W. Śmigaj, C. Rockstuhl, P. Lalanne, and F. Lederer, "Reflection and transmission of light at periodic layered metamaterial film," Phys. Rev. B **84**, 115142 (2011).
32. P. Lalanne, S. Mias, and J. P. Hugonin, "Two physical mechanisms for boosting the quality factor to cavity volume ratio of photonic crystal microcavities," Opt. Express **12**, 458–467 (2004).
33. B. Wang and G. P. Wang, "Plasmon Bragg reflectors and nanocavities on flat metallic surfaces," Appl. Phys. Lett. **87**, 013107 (2005).
34. D. Wang, X. Liu, L. He, Y. Yin, D. Wu, and J. Shi, "Manipulating graphene mobility and charge neutral point with ligand-bound nanoparticles as charge reservoir," Nano Lett. **10**, 4989–4993 (2010).
35. M. Liu, X. Yin, E. Ulin-Avila, B. Geng, T. Zentgraf, L. Ju, F. Wang, and X. Zhang, "A graphene-based broadband optical modulator," Nature **474**, 64–67 (2011).
36. F. Scarpa, S. Adhikari, A. J. Gil, and C. Remillat, "The bending of single layer graphene sheets: the lattice versus continuum approach," Nanotechnology **21**, 125702 (2010).
37. D. B. Zhang, E. Akatyeva, and T. Dumitrică, "Bending ultrathin graphene at the margins of continuum mechanics," Phys. Rev. Lett. **106**, 255503 (2011).
38. V. Atanasov and A. Saxena, "Tuning the electronic properties of corrugated graphene: confinement, curvature, and band-gap opening," Phys. Rev. B **81**, 205409 (2010).